GPPS | JOURNAL

JOURNAL OF THE GLOBAL POWER AND PROPULSION SOCIETY
journal.gpps.global/jgpps

Aeroelastic assessment of a highly loaded high pressure compressor exposed to pressure gain combustion disturbances

Original article

Article history:
Accepted: 16 July 2018
Published: 15 October 2018

This paper is the updated version of a paper originally presented at the GPPS Montreal 18 Conference, in Montreal, May 7–9 2018.

Check for updates

***Correspondence:**
VB: victor.bicalho@ilr.tu-berlin.de

Peer review:
Single blind

Copyright:
© 2018 Bicalho Civinelli de Almeida and Peitsch This is an open access article distributed under the Creative Commons Attribution Non Commercial No Derivatives License (CC BY-NC-ND 4.0). Unrestricted use, distribution, and reproduction of the original work are permitted for noncommercial purposes only, provided it is properly cited and its authors credited. No derivative of this work may be distributed.

Keywords:
aeroelasticity; forced response; unsteady performance; axial compressor; high pressure compressor; pressure gain combustion

Citation:
Bicalho Civinelli de Almeida V., Peitsch D. (2018). Aeroelastic assessment of a highly loaded high pressure compressor exposed to pressure gain combustion disturbances. Journal of the Global Power and Propulsion Society. 2: 477–492.
https://doi.org/10.22261/JGPPS.F72OUU

OPEN ACCESS

Victor Bicalho Civinelli de Almeida[1,*], Dieter Peitsch[1]

[1]*Technical University of Berlin, Marchstr. 12-14, Berlin 10587, BE, Germany*

Abstract

A numerical aeroelastic assessment of a highly loaded high pressure compressor exposed to flow disturbances is presented in this paper. The disturbances originate from novel, inherently unsteady, pressure gain combustion processes, such as pulse detonation, shockless explosion, wave rotor or piston topping composite cycles. All these arrangements promise to reduce substantially the specific fuel consumption of present-day aeronautical engines and stationary gas turbines. However, their unsteady behavior must be further investigated to ensure the thermodynamic efficiency gain is not hindered by stage performance losses. Furthermore, blade excessive vibration (leading to high cycle fatigue) must be avoided, especially under the additional excitations frequencies from waves traveling upstream of the combustor.

Two main numerical analyses are presented, contrasting undisturbed with disturbed operation of a typical industrial core compressor. The first part of the paper evaluates performance parameters for a representative blisk stage with high-accuracy 3D unsteady Reynolds-averaged Navier-Stokes computations. Isentropic efficiency as well as pressure and temperature unsteady damping are determined for a broad range of disturbances. The nonlinear harmonic balance method is used to determine the aerodynamic damping. The second part provides the aeroelastic harmonic forced response of the rotor blades, with aerodynamic damping and forcing obtained from the unsteady calculations in the first part. The influence of blade mode shapes, nodal diameters and forcing frequency matching is also examined.

Introduction

Increase in overall efficiency of aeronautical engines and stationary gas turbines, reducing specific fuel consumption, is being extensively researched. Since traditional engine configurations are reaching saturation development state, novel technological breakthroughs are sought. Among these radical changes, the most significant tackle either the core/bypass flows or the combustor losses. To address core flow hurdles, intercooling, Rankine bottoming and recuperation might be viable options. Reheating is also particularly developed for land-based applications. Concerning bypass losses, geared turbofan and open rotor concepts are receiving considerable attention (Grönstedt et al., 2013, 2016; Gülen, 2017).

With respect to the combustion losses, several innovative approaches have been proposed. Most of them aim at improving current constant-pressure (in fact, pressure-loss) combustion with a pressure-increase process. This so-called pressure gain combustion (PGC) can be

accomplished by different means. The leading paths are pulse detonation (Roy et al., 2004; Pandey and Debnath, 2016), rotating detonation (Zhou et al., 2016; Kailasanath, 2017; Paxson and Naples, 2017), wave rotors (Akbari and Nalim, 2009; McClearn et al., 2016) and shockless explosion (Bobusch et al., 2014; Reichel et al., 2016) combustion. Some other concepts are the piston topping (Kaiser et al., 2015) and the nutating disk (Meitner et al., 2006). All these setups are theoretically supported by substantial thermodynamic gains, described in detail, e.g., by (Heiser and Pratt, 2002; Gray et al., 2016).

Despite fairly different construction and engine-integration characteristics, all these PGC processes introduce additional unsteadiness into the adjacent turbomachinery components, namely, the compressor upstream and the turbine downstream. This unsteadiness is directly linked with the inherently periodic nature of the combustion mechanisms, and affect the operation of both stationary and rotating parts (traditionally designed by steady state workflows). The integration between combustion units and engine (most likely through plena interfaces) is key to estimate proper boundary conditions for the neighboring components, such as perturbation signatures, operation frequencies and amplitudes.

Although fundamental combustion research on pulse detonation had been restricted to low frequency processes, massive increase in the number of ignitions per second has been achieved. Kilohertz pulse detonation frequencies were recently reported by (Taki et al., 2017). As for rotating detonation, it already takes place in the few kilohertz range (Lu and Braun, 2014; Bluemner et al., 2018). Similar periodicity is reported for the other PGC devices. This frequency range is also expected to be pushed up, once PGC technology takes off.

With respect to the amplitudes of such disturbances, they are strongly linked to the PGC operation (such as filling, ignition and purging phases), but also to the plena interfaces. Limited PGC experimental data with upstream measurements is available, such as (Roy et al., 2004; Rasheed et al., 2005). Some numerical work used pressure amplitude values at the combustor interfaces of a few percent up to approximately 40% (Van Zante et al., 2007; Fernelius, 2017; Liu et al., 2017). This disturbance amplitude range is already significant from the turbomachinery point of view, justifying detailed investigations.

The need for assessing the performance and aeroelasticity effects of these disturbances has been recognized by the combustion and turbomachinery academic community (Kailasanath, 2003; Roy et al., 2004; Rasheed et al., 2009; Lu and Braun, 2014; Gülen, 2017). However, quantitative information to evaluate the extent of these changes is scarce, especially for state-of-the-art industrial machines. Up to the current date, there has been no full integration between those PGC cores to commercial engines. Therefore, the current exploratory research sheds some light into the effects of this interfacing (specifically upstream), by numerical means. Both performance and aeroelasticity assessments will be presented.

The manuscript is organized as follows. In the case description section, the simulated high pressure compressor geometry is characterized. Next, the numerical methodologies both for the computational fluid dynamics (CFD) and computational solid mechanics (CSM) are presented. Subsequently, results are given for a broad range of disturbance amplitudes and frequencies, followed by the main outcomes.

Case description

A modern industrial high pressure compressor, depicted in Figure 1 is here used for the simulations (Klinger et al., 2008, 2011). Practical 3D geometries and operation points have been provided by an industrial partner. It is important to say that the whole engine has been designed for traditional deflagration combustion, without specific considerations for PGC and its effects on turbomachinery components. Therefore, the present study analyzes how this traditional setup would potentially react to unsteady disturbances and depart from the reference design.

The simulated domain is the HPC 6th stage, the last with a bladed disk (blisk) design. Although it is not the very last stage right before the combustion chamber, it has been chosen considering that blisk manufacturing becomes increasingly more common in axial compressor design (Peitsch et al., 2005; Honisch et al., 2012; Mayorca et al., 2012; Zhao et al., 2015). Due to confidentiality constraints, the speedline itself and some absolute design quantities will not be disclosed here, but rather normalized values, enough for full comprehension and comparative evaluations.

Numerical methodology

For brevity purposes, neither the fluid nor the solid domain state and constitutive equations will be derived here. Rather, focus will be given to the interface treatment of necessary aeroelastic quantities, such as aerodynamic work or pressure harmonics. The next sections describe respectively the CFD (steady and unsteady) and CSM

Figure 1. The E3E high pressure compressor rotor.

methodologies used along this work. The space and time independence studies for the grids are likewise presented.

Computational fluid dynamics

Due to the unsteady behavior associated with the new combustion processes, 3D unsteady viscid fluid dynamics simulations are employed, both in time and frequency domain. Time-domain calculations are here used to determine performance parameters, unsteady damping and blade surface pressure harmonics, to be later used in the structural simulations. Frequency-domain runs determine the aerodynamic damping.

(i) Steady state: the Navier-Stokes equations are boundary-layer resolved with the finite volumes solver CFX® (ANSYS Academic Research, Release 18.1), with air (ideal gas) as compressible medium. Fourth-order Rhie & Chow smoothing is employed (Rhie and Chow, 1983), while Reynolds stresses are computed by the two-equation Menter's SST turbulence model (Menter, 1994). Since the simulated stage is located substantially far from the engine inlet, the flow is safely assumed to be fully turbulent, so no transition models were shown necessary. Double-precision, properly converged steady state solutions (with root-mean-square residuals lower than 10^{-5}, and imbalances lower than $5{\cdot}10^{-6}$) are used as initial conditions for the unsteady runs.

The 3D geometries were meshed with AutoGrid5® developed by Numeca (IGG™/AutoGrid5™ v11.1). Both root fillet and tip gap have been modeled. Multi-block structured hexaedra meshes were employed, with directional boundary-layer refinement on all walls (dimensionless wall distance $y^+ \approx 1$), keeping the expansion ratio below 1.2. The topology for both rotor blades and stator vanes is the O4H. The tip gap was modeled with at least 30 cells in the radial direction.

Several meshes were generated in order to perform a proper grid independence study, done separately for rotor and stator. The grids were refined as uniformly as practical, however always keeping the boundary layer on the walls resolved. Figure 2 displays three chosen meshes for rotor (labeled from coarsest to finest as R-A, R-B and R-C) and stator (labeled as S-A, S-B and S-C), with isentropic efficiency and mass flow values normalized by the finest grid, as a function of cell count. The deviation between the finest- and coarsest-grid values is less than 1% for both domains, in the sense that all displayed grids capture the global flow behavior accurately enough. The Grid Independence Index (Celik, 2008), formally derived based on the Richardson extrapolation (Roache, 1994), has been calculated and showed no oscillatory behavior. For the isentropic efficiency, the index between finest and medium meshes is $GCI_{BC} = 0.24\%$, with apparent order of 1.94. The grids utilized for the current stage are assembled together and shown in Figure 3. The number of nodes for the stage (if using one passage for rotor and one for stator) is approximately 1.3 million.

As inlet boundary conditions, total pressure and temperature along with flow direction are implemented, while on the outlet the static pressure is prescribed. Both on inlet and outlet, radial profiles experimentally validated by the manufacturer are utilized. For the steady runs *only*, mixing-plane interface, with constant total pressure (that is, no loss in through the interface), is used to account for the non-unitary pitch ratio.

(ii) Unsteady: two types of time-resolved simulations are performed, with and without the PGC disturbances. The time discretization scheme utilized is the second order backward Euler, with a bounded high-resolution

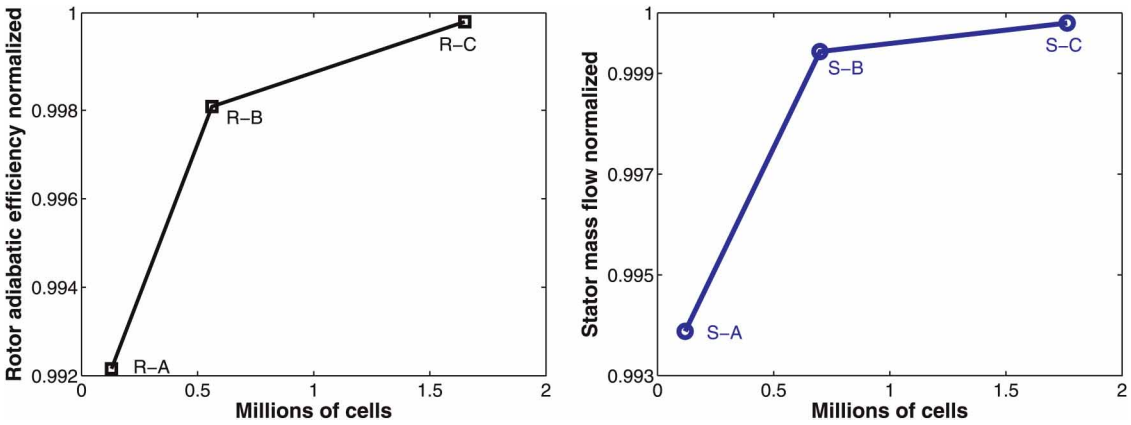

Figure 2. Grid independence study for fluid system, normalized by finest grid values.

discretization for advection and viscous terms. The solution is deemed periodically converged when the relative difference between two consecutive periods for some globally integrated parameter (such as compression ratio or efficiency) or pressure probe falls below 0.05%. The attainment of quasi-convergence depends not only on the blade passing frequency (BPF), but also on the combustion-originated frequency and intensity, which in turn determines the required total run time.

The time resolution must be properly chosen to model the necessary phenomena without excessively consuming computational resources. For the present case, the main (a priori known) frequencies to be modeled by the time march are the rotor BPF and the disturbance frequency. A temporal resolution study was performed to determine the minimum time discretization required, using the number of time steps per rotor passing period (TSRPP) as a parameter. Pressure time traces of two points located between rotor and stator (one in each domain, respectively P1 and P2) are shown in Figure 4 (after periodic convergence is achieved). For both domains, 50 TSRPP are enough to accurately capture the unsteady behavior. To enhance resolution for the disturbed runs, a slightly higher value of 55 TSRPP has been chosen.

It is important to highlight that, under unsteady disturbances (additional to the rotor-stator frequency), the required time step could become smaller. To assess whether 55 TSRPP is enough for the outlet disturbance with the highest frequency here simulated (3.0 times the BPF), an extra run with halved time step (i.e., 110 TSRPP) was carried out, for an extra full rotor revolution. In comparison with the 55 TSRPP setup, a relative difference of 0.09% and 0.005% for isentropic efficiency and compression ratio, respectively, was found. Unsteady damping, as well as modal forcing (both defined further), showed similar minimal changes. From that, the current time resolution was deemed enough within the simulated disturbance range. Higher frequency disturbances could possibly require further time step refinement.

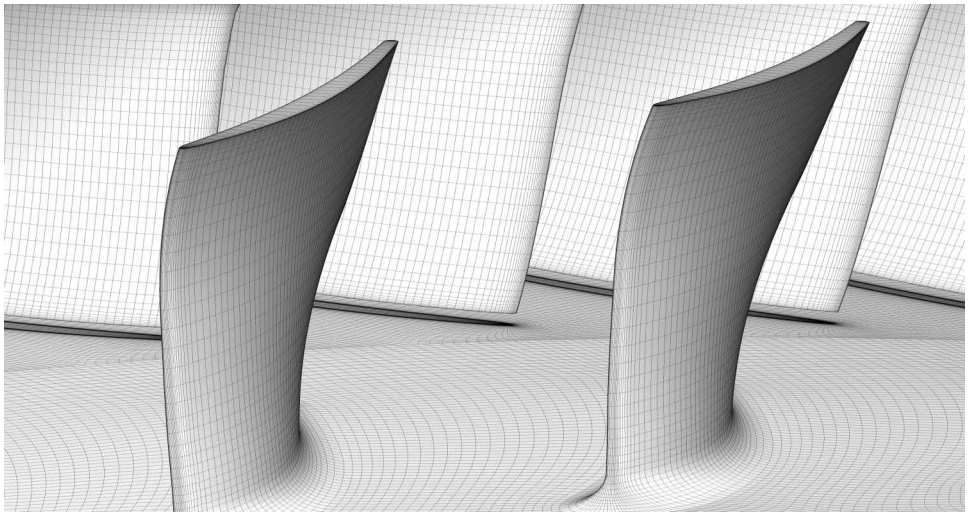

Figure 3. Grids R-B and S-B for the simulated stage (rotor on the front and stator on the back), obtained after grid independence study. Geometry is rescaled.

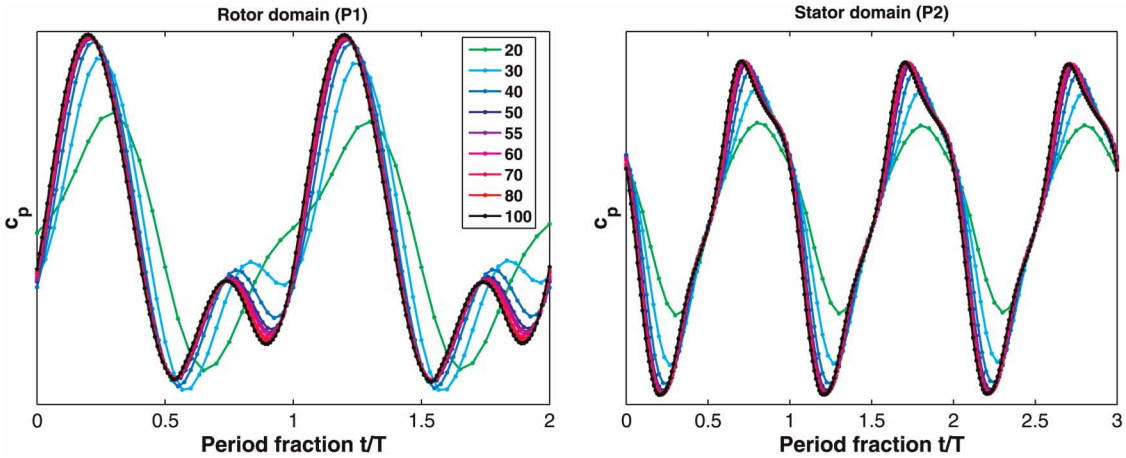

Figure 4. Pressure probe periodically converged time trace, on rotor (P1) and stator (P2) domains. Several values for time steps per rotor passing period (TSRPP) are shown.

For the transient calculations, the number of rotor blades was reduced by one unit, so that 3 rotor passages and 4 stator passages yield a unitary pitch ratio. This modification prevents phase errors which would incur when using for example the profile-scaling method (Galpin et al., 1995). Time-inclining or -shifted methods, such as (Giles, 1988) or (Gerolymos et al., 2002), are not physically consistent when disturbance frequencies different from the BPF are present in the system. In summary, the current unsteady simulation setup does not induce frequency or phase errors due to non-unitary pitch ratio, with sliding meshes accurately modeling the transient phenomena that takes place between rotor and stator. All unsteady disturbances are modeled by the time marching scheme without further simplifications. The total number of nodes for this setup is approximately 4.6 million.

To model the PGC disturbances, time periodic boundary conditions at the stage outlet have been implemented. To the knowledge of the authors, no effective test rig or prototype coupling industrial axial compressor and turbine to a pressure gain combustor has been built, in a fully coupled fashion. Ongoing investigations focus on how to connect these components through adequate plena geometries, to minimize unsteadiness and therefore prevent extra losses. Accordingly, due to the lack of more precise plenum information, it is assumed that the unsteadiness reaching the compressor/combustor interface does not vary circumferentially, being here described by harmonic fluctuations, as in Equation (1).

$$p(\mathbf{x}, t) = p(\mathbf{x})[1 + A_d \cdot \sin(2\pi f_d t)] \tag{1}$$

Here, A_d and f_d stand respectively for amplitude and frequency of the imposed harmonic disturbance on the static pressure distribution $p(\mathbf{x})$. Indeed, since the pressure is in this work prescribed radially, $p(\mathbf{x}) = p(r)$ for radius r. This approach assumes that the number of blades and vanes is rather larger than the number of combustion units downstream, so that no disturbance wave interaction among combustor units is modeled.

(iii) Time-spectral: the frequency-domain method employed here is the nonlinear harmonic balance (Hall et al., 2002) (also known as time spectral method (Gopinath and Jameson, 2005)). The time and spatial dependent state variables are written as a Fourier series for a predetermined fundamental frequency, whose first harmonics are iteratively and simultaneously solved with a pseudo time march. Along this work, 3 harmonics (producing 7 time levels) have been used, after parametric studies showed that more harmonics did not change the solution substantially. Additionally, 20 pseudo time steps per oscillation period were enough to achieve the desired computational accuracy at rapid convergence. The nonlinear harmonic balance is here utilized to determine the aerodynamic work W_{aero}, as defined in Equation (2).

$$W_{\text{aero}} = \int_t^{t+T} \int_\ell p\mathbf{v} \cdot \hat{\mathbf{n}} d\ell dt \tag{2}$$

Here, p is the static pressure, $\mathbf{v}$ the wall velocity vector and $\hat{\mathbf{n}}$ the wall outwards pointing normal versor. The surface integral takes place along the blade walls ℓ. The aerodynamic work is integrated in time t during one

period T. For negative W_{aero}, energy is being fed from the blade motion into the fluid stream, in a stable fashion; for positive W_{aero}, energy is being transferred from the fluid to the structure, hinting instability. This is the same approach to assess flutter stability, based on the well-established energy method (Carta, 1967), with traveling-wave configuration (Lane, 1956; Platzer et al., 1987). Interblade phase angles are here symbolized by σ. The wall movement is prescribed according to the desired rotor blade mode shape. More details will be further given in the modal analysis section.

With this approach, extensively used in industrial design, two assumptions are implied: constant vibration frequency (for each natural mode) and independence between damping and forcing (justified, for example, by (Mao and Kielb, 2017)). It is important to remark that the main vibration damping contribution for a blisk structure comes from aerodynamic forcing, since friction damping is not present, and material damping is negligible. Therefore the need of precisely determining the aerodynamic work on the rotor blade.

The aerodynamic work is used to compute the damping ratio ξ, as in Equation (3) (see for example (Saiz, 2008; Schrape et al., 2008; Zhang et al., 2012)).

$$\xi = \frac{-W_{aero}}{2\pi\omega^2 q^2} \tag{3}$$

Here, $\omega = 2\pi f$ is the angular vibration frequency of the blade (obtained from a prestressed modal analysis), and q is the scaling factor of the natural mode shape for the CFD computation (including the modal scaling, in case mode shapes are obtained as mass normalized).

The time-spectral analyses simulate the rotor domain only, with the same inlet boundary conditions as for the stage runs (total pressure, total temperature and flow direction). Regarding the rotor outlet, design static pressure radial profiles for the corresponding axial position (validated by the manufacturer) are employed.

In this work, the rotor blades (which in general are under more mechanical stresses than the stator) vibrate on the first three natural frequencies (the most energetic, sufficient for aeroelastic structural response (Silkowski and Hall, 1997; Piperno and Farhat, 2001; He, 2010)), with a maximum tip displacement set to 0.5% of blade height. The normalization provided by Equation (3) makes sure that the damping ratio is independent of the chosen scaling factor q, within the quadratic regime. Parametric simulations have confirmed that the chosen values for the scaling factor and natural frequencies lie within the proportionality range expressed by Equation (3).

Computational solid mechanics

(i) Prestressed static and modal analyses: the current rotor blisk is modeled as a cyclic symmetric sector, with a typical modern industrial titanium alloy. Here, focus will be given to the blade geometry and mesh, sufficing to say that the disk displacement is fixed at the bore, that is, shaft flexibility is ignored, as standard with blisk analyses (Sever, 2004; Li et al., 2016). In the prestressed static analysis, constant rotational velocity and the mean static pressure on the blade surface are prescribed as loads. The pressure load comes from CFD-only simulation without any external disturbance, that is, a baseline unsteady run. The nodal pressure time history on the blade surface is expanded into a Fourier series, whose first term correspond to the mean static load (which is used in the prestressed static analysis). The following terms determine the engine order multiples (these shall be later used in the harmonic response analyses).

The finite elements method (FEM) solver ANSYS® (ANSYS Academic Research, Release 18.1) has been used for the structural analyses. After preliminary studies comparing different finite elements families, high-order tetrahedra have been chosen in place of hexaedra, pyramids or wedges. Although hexaedra could facilitate the mapping between solid and fluid grids, tetrahedra elements have proven to better model the current physics of the problem, particularly because regions with high stress gradients are better meshed. Similarly to the fluid domain, a grid independence study was performed for the solid meshes, this time with the first natural frequencies as comparative parameters. The grid convergence for two modes is displayed in Figure 5.

Even the coarsest of the generated meshes represents remarkably good the displayed modes (very similar behavior takes place for the first 20 mode shapes). However, the last but one finest mesh (labeled as Blisk-D) has been chosen to guarantee a good mapping between fluid and solid system variables. Each blade sector has 96322 nodes. This grid, expanded to cover the whole blisk, is shown in Figure 6, contoured with the second blade natural mode displacement, with 40 nodal diameters.

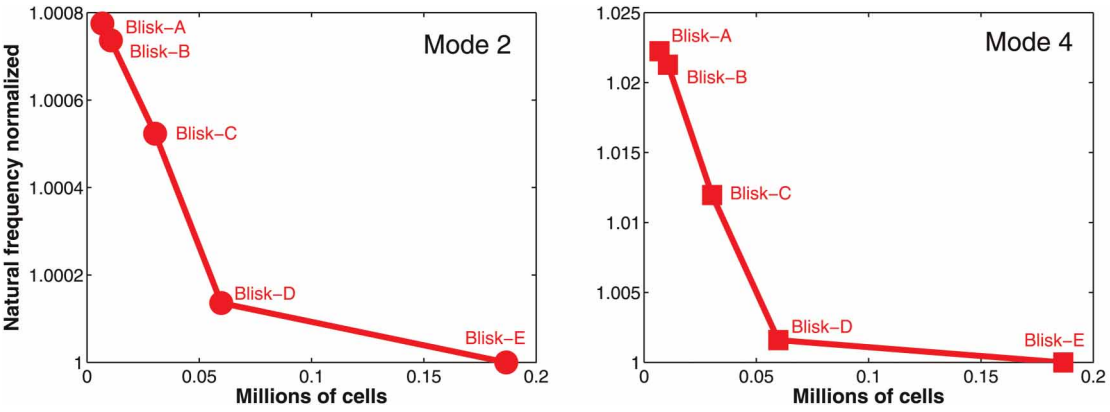

Figure 5. Grid independence study for solid system, normalized by finest grid values.

For brevity purposes, only a brief remark is made about the use of cyclic symmetry. In order to prevent the expensive modeling of the whole blisk structure, just one sector is meshed. Fourier decomposed boundary conditions are implemented on the symmetrical faces in the circumferential direction, with proper consideration of the total number of sectors (Thomas, 1979; Balasubramanian et al., 1991).

(ii) Harmonic forced response: subsequently to the prestressed modal analyses, mode-superposition harmonic response is computed. The time and frequency domain relations are displayed in Equation (4).

$$\begin{aligned} \mathbf{M}\ddot{\mathbf{U}}(t) + \mathbf{C}\dot{\mathbf{U}}(t) + \mathbf{K}\mathbf{U}(t) &= \mathbf{F}(t) \\ \ddot{d}_j(\omega) + 2\omega_j\xi_j\dot{d}_j(\omega) + \omega_j^2 d_j(\omega) &= f_j(\omega) \end{aligned} \tag{4}$$

Here, as in classic FEM, **M**, **C** and **K** are the mass, damping and stiffness matrices, plus the displacement and forcing vectors **U** and **F**. Note that, since the forcing vector $\mathbf{F}(t)$ is complex when expanded into a harmonic series, real and imaginary aerodynamic forcing components must be inputted. Equation (4) shows the nodal coordinate $d_j(\omega)$ for one general natural mode j with corresponding frequency ω (more details given by (Fu and He, 2001; Saiz, 2008)). Both the complex-valued forcing $f_j(\omega)$ from the unsteady time-domain runs and the damping ratio (ξ_j from Equation (3)) from the frequency-domain runs are used, in order to obtain the maximum stresses and strains on the blisk.

In the mode-superposition harmonic analyses, the first 117 natural modes have been used. A phase sweep was done, according to the studied target-frequency. The highest natural frequency obtained in the modal analysis setup was always at least 1.5 times the excitation frequency.

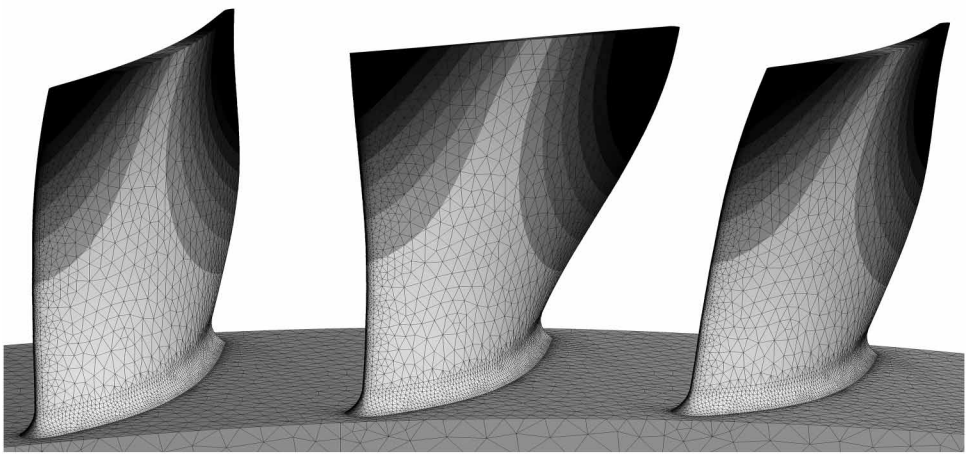

Figure 6. Grid Blisk-D for the simulated rotor, obtained after grid independence study. Whole-circle expanded result displays the second blade natural mode (torsion) contours. Geometry is rescaled.

Results

Computational fluid dynamics

In this subsection, the CFD-only results are presented. Initially, time-domain calculations are assessed, showing how the disturbances affect performance, as well as the unsteady damping. Next, the frequency-domain results for aerodynamic damping are given.

(i) Performance drop: the isentropic efficiency of the simulated stage was calculated for several disturbances patterns. Outlet static pressure amplitude and frequency have been varied according to current (and foreseen) PGC ranges. The amplitude A_d is normalized as a percentage of the outlet mean static pressure, while the frequency is written as a function of both BPF multiple and Strouhal number St. The last is defined here as $\mathrm{St} = (f_d c_r)/v_{\mathrm{axial}}$, where c_r is a reference rotor chord length and v_{axial} the mass-flow-averaged inlet axial velocity (Liu et al., 2017). Figure 7 depicts the drop in stage isentropic efficiency η as a function of disturbance frequency and amplitude.

As a first trend, higher disturbance amplitudes A_d lead to larger drops in η. This behavior is to some extent expected once the flow conditions depart from the steady state design. However, for low disturbance frequencies (such as 0.125 and 0.25 times the BPF), η decrease is evidently larger, reaching more than 15% for $A_d = 20\%$. This performance depletion should be accounted for, when designing a compressor stage for a particularly perturbed environment. Although small decreases in efficiency might not represent a setback for the use of unsteady combustion, higher disturbance amplitudes, especially at lower frequencies, can lead to flow separation on the blade surface, being profoundly detrimental for stable compressor operation. This was the case for lower disturbance frequencies, such as $f_d = 25\%$ BPF and $A_d = 20\%$, where, due to the disturbance waves, the adverse pressure gradient increases on the stator, followed by the rotor, inflating recirculation areas adjacent to the blade (see Figure 8, depicting the static entropy and surface streamlines around the rotor blade, at the same time instant for the undisturbed and the disturbed cases). These recirculation areas adjacent to the blade surface are not present in the undisturbed transient instance. This performance depletion region is also indicated at the upper left corner on the efficiency drop map in Figure 9.

(ii) Unsteady damping ϵ: this quantity is defined in Equation (5).

$$\Delta\phi = \frac{\phi_{\max} - \phi_{\min}}{\phi_{\mathrm{mean}}}$$
$$\epsilon = \frac{\Delta\phi_2 - \Delta\phi_1}{\Delta\phi_2} \tag{5}$$

$\Delta\phi$ represents the periodic variation of any (properly space-averaged) quantity in time, normalized by its mean. ϕ can be any state variable, being restricted in this manuscript to (total and static) pressure and temperature. This definition is similar to the one given by Liu et al. (2017) (however, since the disturbances now propagate upstream, the order of the streamwise-station indexes 1 and 2 is reversed). The unsteady damping

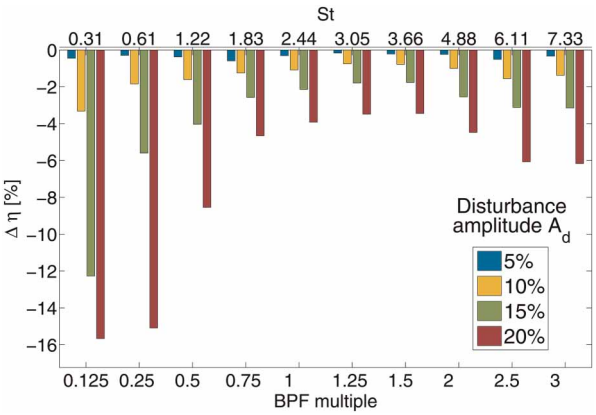

Figure 7. Isentropic efficiency variation as a function of disturbance frequency (function of St and BPF multiple). Results for several disturbance amplitudes.

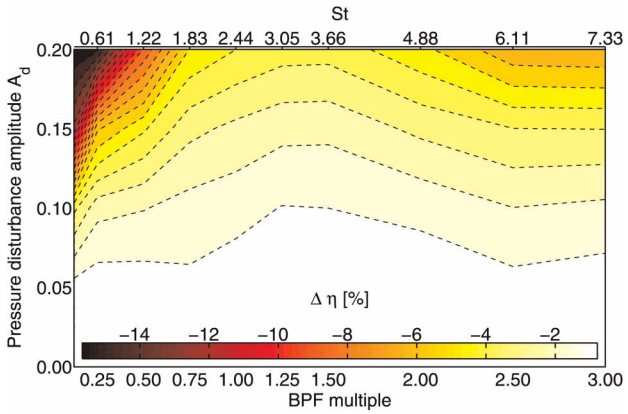

Figure 8. Isentropic efficiency variation map, as function of disturbance frequency and amplitude.

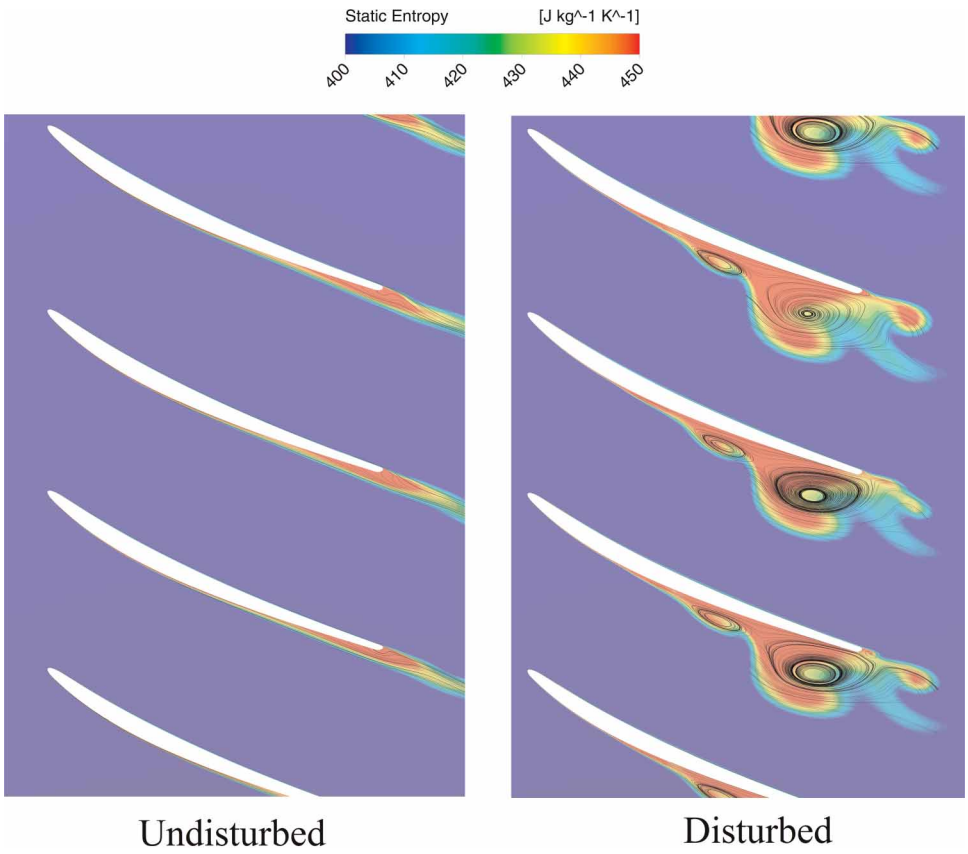

Figure 9. Static entropy contour and surface streamlines around the rotor blade (cross section), for undisturbed and disturbed cases, with disturbance frequency of 0.25 BPF and amplitude 20%. A substantial increase in entropy and recirculation zones is present in the disturbed run. Geometry is rescaled.

computation is carried out for a few periods (the longest among disturbance and blade passing periods), and only after the unsteady run has achieved proper periodic convergence as previously described. The streamwise stations are set right before and after each blade/vane (circa 10% of chord).

The essence of the unsteady damping is to determine how much a state property unsteady variation is reduced ($\epsilon > 0$) or amplified ($\epsilon < 0$), as it travels from stations 2 to 1. Note that the unsteady damping is completely unrelated to the aerodynamic damping (presented in the next section). Figure 10 depicts the unsteady damping for total pressure and temperature, at $A_d = 20\%$, along the whole stage (that is, in this case station 2 is right aft stator vane and station 1 right fore rotor blade).

All unsteady damping values obtained are positive and close to 1 (that is, almost complete attenuation). Static and total unsteady damping show very similar behavior. However, very low and very high frequencies are less damped than the ones close to the BPF, when the disturbance propagates farther upstream. This is a valuable

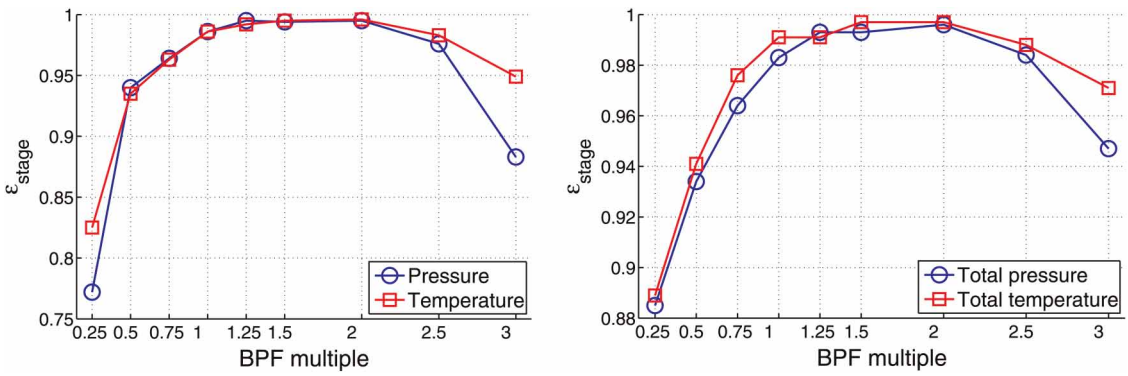

Figure 10. Unsteady damping for disturbance amplitude of 20%. Pressure and temperature (static and total) values shown for several frequencies.

information for the aeroelasticity designer, since the blade structure should avoid (or at least withstand) vibrations at the adjacent excitation frequencies. The unsteady damping pinpoints how far the unsteadiness propagates along the streamwise direction, with high values (say, more than 95%) indicating that these fluctuations are weak enough when reaching the next stage, and therefore do not necessarily prompt redesign considerations.

(iii) Aerodynamic damping: the aerodynamic work was used to determine the damping ratio ξ, according to Equations (2) and (3). The first three natural blade modes were simulated with the nonlinear harmonic balance, along the whole nodal diameter (conversely, interblade phase angle) range. These mode shapes are depicted in Figure 11. A sample result is shown in Figure 12, for the second blade natural mode (torsion) with 40 nodal diameters ($\sigma \approx 177°$) traveling forward. One can see that the wall power density contours are similar to the mode displacement contours shown in Figure 6, indicating good FEM-CFD mapping and also that the energy exchange distribution due to blade motion relates, in this case, directly to the mode shape itself.

Subsequently, the damping ratio was calculated from the aerodynamic work, shown in Figure 13. Firstly, all simulated modes were shown to be stable for all nodal diameters (that is, $\xi > 0$). Secondly, all mode shapes present a relatively smooth harmonic behavior (mostly on its first order), as predicted by the aerodynamic influence coefficient theory, in traveling wave mode setups (Platzer et al., 1987; Vogt, 2005). The minimum damping ratio from the simulated natural frequencies will be used in the harmonic response analyses, as a conservative measure.

Computational solid mechanics

After the prestressed modal analysis, the next step is to identify the frequencies and forcing shapes which excite the structure. For these loads, the Campbell and interference diagrams, respectively, are convenient. Due to the exploratory character of this study, several cases have been run, however restricted to the nominal rotational speed of the machine.

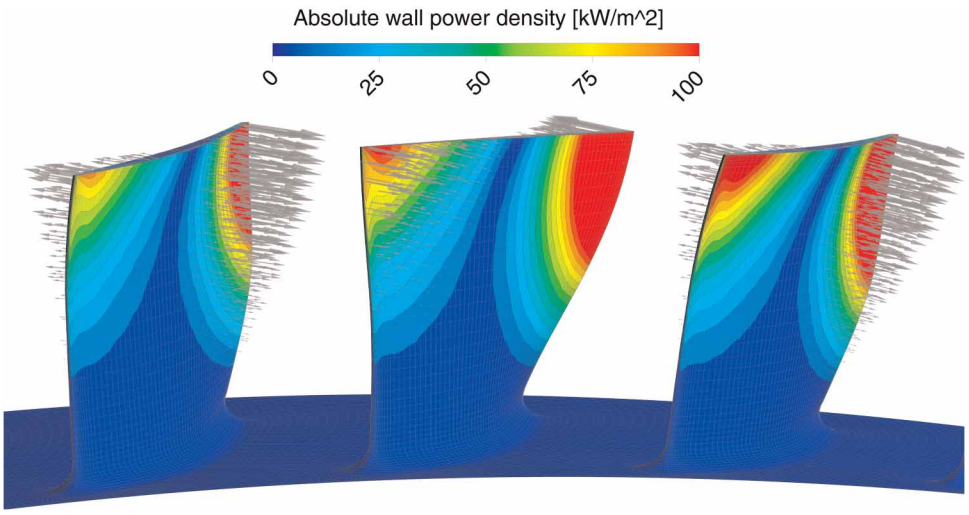

Figure 11. Power density on blade wall, for second blade natural mode (torsion), 40 nodal diameters, as a forward traveling wave. Mesh velocity vectors are also displayed (exaggerated displacement for visualizing purposes). Geometry is rescaled.

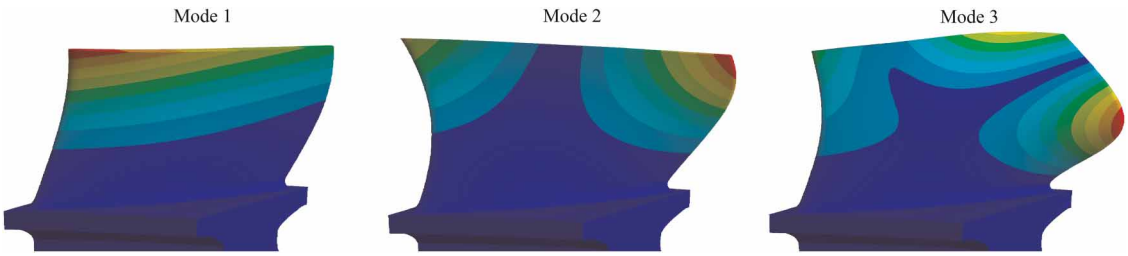

Figure 12. Displacement contours of first three blade-dominated natural modes. Geometry is rescaled.

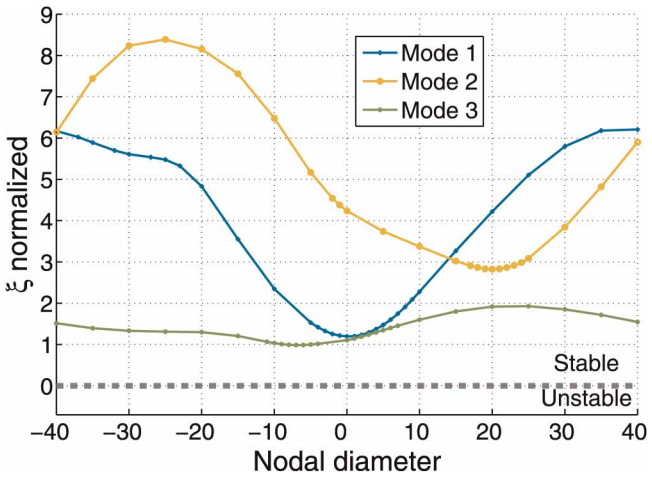

Figure 13. Normalized damping ratio, as a function of nodal diameter.

Along this manuscript, focus is cast on the disturbances originated from the combustor, although the stator perturbation (as seen by the rotor) is also naturally calculated. On that account, a sample interference diagram is shown in Figure 14, with five circumferentially scattered disturbance units downstream of the stage (which could correspond to detonation tubes, rotating-detonation chambers etc.). The inclination of the rotational speed line is determined not only by how fast the shaft spins, but also by the number of disturbance units. Therefore, for each choice of combustor units downstream, a new interference diagram is produced. The integral crossings between the speedline and the natural frequencies indicate which nodal diameter shapes are expected to be excited (Wildheim, 1979; Bertini et al., 2014).

The simulated engine orders are directly correlated with the excitation frequency f_d. A Fourier decomposition of the transient pressure signal (from the CFD runs) was performed for each one of the disturbance frequencies. The sampling rate and interval was regarded so to achieve the proper Nyquist frequency, considering again the longest among disturbance and blade passing periods. In general, a full wheel rotation produced periodically converged results enough to cover several multiples of the Nyquist frequency. It is important to check the transient signal to be used for the Fourier decomposition specially for the lower disturbance frequencies.

Figure 15 shows the maximum von-Mises stresses on the rotor blade for the undisturbed and the disturbed case, for $f_d = 0.125$ BPF run with $A_d = 20\%$. The disturbed case shows clearly a stress distribution much higher than the undisturbed, particularly close to the root leading edge, right above the fillet. For this specific disturbance frequency, the first natural mode (bending) is the one most excited.

The maximum von-Mises stress on the rotor blisk is shown in Figures 16 and 17, for the disturbed computations. The normalization was done in two different ways. In Figure 16, all stresses were divided by the stress obtained in the 1.0 BPF disturbed run (any other value could be arbitrarily chosen, which would change only

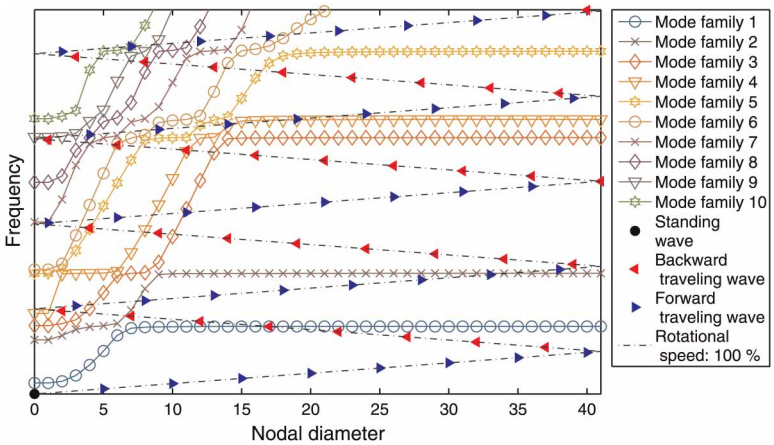

Figure 14. Sample interference diagram for simulated blisk, with the first ten mode shape families. An illustrative rotational speed line is indicated, for clear visibility purposes.

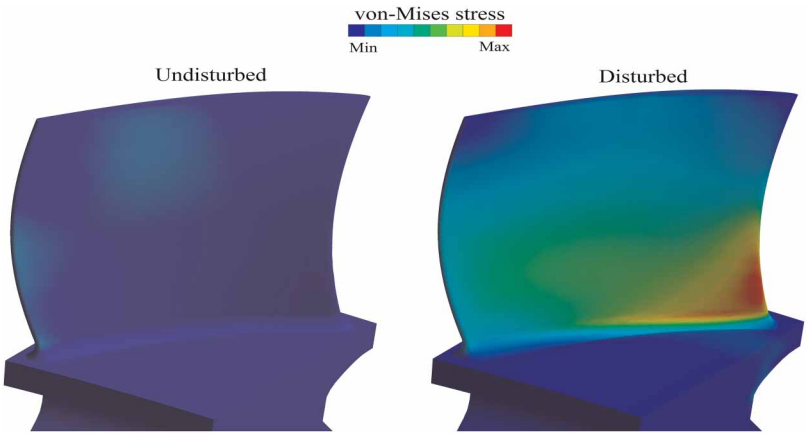

Figure 15. Normalized von-Mises stresses on rotor blade for undisturbed and disturbed cases. The disturbance frequency is 0.125 BPF with amplitude 20%. Geometry is rescaled.

the vertical axis scale). The observed behavior matches qualitatively with the drop in efficiency, as well as the unsteady damping plots (depicted respectively in Figures 7 and 10). The stronger disturbance propagation observed in the low-frequency range excites the rotor blade more than the higher frequencies. Therefore, larger displacements and stresses are expected.

With respect to Figure 17, the normalization is accomplished dividing the maximum von-Mises stresses by the corresponding values obtained in the counterpart undisturbed runs. This is done independently for each excitation frequency. Low disturbance frequencies, again, promote higher stresses on the blade. The high values are expected, considering that, for the baseline undisturbed case, the strain induced on the blade due to the specified excitation frequencies is indeed minimal (except if specifically adjacent to BPF's or eventual system fluctuations, such as rotating instabilities, are present). On the other hand, for the disturbed runs, the Fourier decomposition of the pressure will invariably yield much higher values close to the exciting frequencies. In spite of large relative values, the dynamic stress still remains under acceptable material limits (at least for the disturbance amplitudes here considered).

Conclusions

Numerical aeroelastic and high-accuracy CFD analyses were presented in this work, contrasting undisturbed and pressure gain disturbed operation of a typical industrial high pressure compressor stage. Due to the exploratory nature of this study, a wide range of disturbance frequencies and amplitudes was considered. The principal outcomes are:

(i) From the turbomachinery component performance viewpoint, decrease in stage isentropic efficiency η of more than 15% (for pressure disturbance amplitude of $A_d = 20\%$ and frequency $f_d = 0.125$ BPF) was observed. Additionally, momentary strengthening in recirculation zones adjacent to the blade surface (due to the increase in the adverse pressure gradient), also occurred for the lower frequencies.

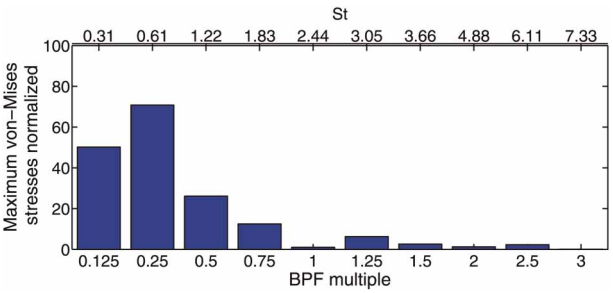

Figure 16. Maximum von-Mises stresses on rotor blade for disturbed runs. Values normalized by the 1.0 BPF disturbance frequency results.

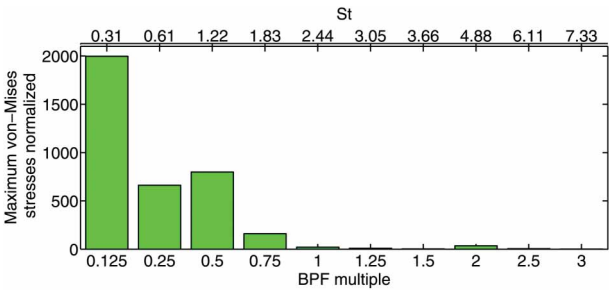

Figure 17. Maximum von-Mises stresses on rotor blade for disturbed runs. Values normalized by the undisturbed results for each respective frequency.

Finally, η drop was shown to be squarely proportional to the relative variation in outlet pressure, for the simulated range.

(ii) The pressure and temperature unsteady damping (as defined in Equation (5)) was higher than 95%, for disturbance frequencies between 0.75 and 2.5 multiples of the BPF. Lower frequencies are particularly less unsteadily damped, meaning that the propagating disturbance should be perceptible to a greater extent upstream of the simulated stage.

(iii) The aerodynamic damping calculations exhibited no unstable nodal diameter for the operating point. The first three modes simulated with the nonlinear harmonic balance method displayed a fairly sinusoidal-like smooth behavior along the interblade phase angle spectrum. The global damping ratio ξ was calculated from the aerodynamic work to be further used in the harmonic response analyses.

(iv) After a prestressed modal run, the rotor blisk was excited with the unsteady Fourier transformed forces, on mode-superposition harmonic response analyses. The horizontal comparison between different excitation frequencies followed the same behavior of the efficiency drop and unsteady damping. That is, the upstream propagating disturbances excite the rotor blade substantially more on the low-frequency end. Additionally, the von-Mises stresses obtained with the disturbed runs, anew for the lower frequencies, were several hundred times higher than the corresponding stresses for the undisturbed cases. For excitation frequencies higher than 1 BPF, this stress magnification is much more modest. Nonetheless, the stresses in all cases were still below material limits.

Nomenclature

A_d disturbance amplitude
$\mathbf{C}$ damping matrix
c reference chord
d complex modal coordinate
$\dot{d}$ overdot for time derivative ($\dot{d} = \partial d/\partial t$)
f complex modal forcing
f_d disturbance frequency
$\mathbf{K}$ stiffness matrix
ℓ surface integration coordinate
$\mathbf{M}$ mass matrix
$\hat{\mathbf{n}}$ normal versor
p pressure
q scaling factor for FEM-CFD mapping
r radius
St Strouhal number ($\mathrm{St} = f_d c_r / v_{\mathrm{axial}}$)
t time
T period
$\mathbf{U}$ displacement vector
$\mathbf{v}$ velocity vector
$\mathbf{x}$ spatial coordinates vector
W_{aero} aerodynamic work
y^+ dimensionless wall distance

Greek

ϵ unsteady damping
η isentropic efficiency
ξ damping ratio
σ interblade phase angle
ϕ generic state variable
ω angular frequency of vibration

Subscripts

1 streamwise station numbering
d disturbance

j natural mode index
r rotor
s stator

Abbreviations

BPF blade passing frequency
CFD computational fluid dynamics
CSD computational solid dynamics
FEM finite elements method
GCI_{BC} grid independence index for grids B and C
HPC high pressure compressor
PGC pressure gain combustion
TSRPP time steps per rotor passing period

Acknowledgements

The authors greatly acknowledge Rolls-Royce Deutschland Ltd & Co KG. for providing the test case data. We acknowledge support from the German Research Foundation and the Open Access Publication Funds of TU Berlin, Germany.

Funding sources

Berlin International Graduate School in Model and Simulation based Research (BIMoS), Germany, Bicalho Civinelli de Almeida.

Competing interests

The authors declare that they have no conflict of interest.

References

Akbari P. and Nalim R. (2009). Review of recent developments in wave rotor combustion technology. Journal of Propulsion and Power. 25: 833–844. https://doi.org/10.2514/1.34081

ANSYS Academic Research, Release 18.1 (n.d) (Report).

Balasubramanian P., Jagadeesh J. G., Suhas H. K., and Ramamurti V. (1991). Free-vibration analysis of cyclic symmetric structures. Communications in Applied Numerical Methods. 7: 131–139. https://doi.org/10.1002/cnm.1630070207

Bertini L., Neri P., Santus C., Guglielmo A., and Mariotti G. (2014). Analytical investigation of the SAFE diagram for bladed wheels, numerical and experimental validation. Journal of Sound and Vibration. 333: 4771–4788. https://doi.org/10.1016/j.jsv.2014.04.061

Bluemner R., Bohon M. D., Paschereit C. O., and Gutmark E. J. (2018). Single and Counter-Rotating Wave Modes in an RDC. In: 2018 AIAA Aerospace Sciences Meeting.

Bobusch B. C., Berndt P., Paschereit C. O., and Klein R. (2014). Shockless explosion combustion: An innovative way of efficient constant volume combustion in gas turbines. Combustion Science and Technology. 186: 1680–1689. https://doi.org/10.1080/00102202.2014.935624

Carta F. O. (1967). Coupled blade-disk-shroud flutter instabilities in turbojet engine rotors. Journal of Engineering for Gas Turbines and Power. 89: 419–426. https://doi.org/10.1115/1.3616708

Celik I. B. (2008). Procedure for Estimation and Reporting of Uncertainty Due to Discretization in CFD Applications. Journal of Fluids Engineering. 130: 078001. https://doi.org/10.1115/1.2960953

Fernelius M. H. (2017). Experimental and Computational Analysis of an Axial Turbine Driven by Pulsing Flow (Report).

Fu Z.-F. and He J. (2001). Modal analysis. Butterworth-Heinemann, Oxford, UK.

Galpin P. F., Broberg R. B., and Hutchinson B. R. (1995). Three- Dimensional Navier Stokes Predictions of Steady-State Rotor/Stator Interaction with Pitch Change. In: 3rd Annual Conference of the CFD.

Gerolymos G. A., Michon G. J., and Neubauer J. (2002). Analysis and application of chorochronic periodicity in turbomachinery rotor/stator interaction computations. Journal of Propulsion and Power. 18: 1139–1152. https://doi.org/10.2514/2.6065

Giles M. B. (1988). Calculation of unsteady wake/rotor interaction. Journal of Propulsion and Power. 4: 356–362. https://doi.org/10.2514/3.23074

Gopinath A. and Jameson A. (2005). Time Spectral Method for Periodic Unsteady Computations over Two- and Three- Dimensional Bodies. 43rd AIAA Aerospace Sciences Meeting and Exhibit.

Gray J. A. T., Vinkeloe J., Moeck J., Paschereit C. O., Stathopoulos P., et al. (2016). Thermodynamic Evaluation of Pulse Detonation Combustion for Gas Turbine Power Cycles. Volume 4B: Combustion, Fuels and Emissions.

Grönstedt T., Irannezhad M., Lei X., Thulin O., and Lundbladh A. (2013). First and Second Law Analysis of Future Aircraft Engines. Volume 2: Aircraft Engine; Coal, Biomass and Alternative Fuels; Cycle Innovations.

Grönstedt T., Xisto C., Sethi V., Rolt A., García Rosa N., et al. (2016). Ultra Low Emission Technology Innovations for Mid-Century Aircraft Turbine Engines. Volume 3: Coal, Biomass and Alternative Fuels; Cycle Innovations; Electric Power; Industrial and Cogeneration; Organic Rankine Cycle Power Systems.

Gülen S. C. (2017). Pressure gain combustion advantage in land-based electric power generation. Journal of the Global Power and Propulsion Society. 1: 288–302. https://doi.org/10.22261/JGPPS.K4MD26

Hall K. C., Thomas J. P., and Clark W. S. (2002). Computation of unsteady nonlinear flows in cascades using a harmonic balance technique. AIAA Journal. 40: 879–886. https://doi.org/10.2514/2.1754

He L. (2010). Fourier methods for turbomachinery applications. Progress in Aerospace Sciences. 46: 329–341. https://doi.org/10.1016/j.paerosci.2010.04.001

Heiser W. H. and Pratt D. T. (2002). Thermodynamic cycle analysis of pulse detonation engines. Journal of Propulsion and Power. 18: 68–76. https://doi.org/10.2514/2.5899

Honisch P., Strehlau U., and Kühhorn A. (2012). Modelling of industrial blade integrated disks (blisks) with regard to mistuning. In: 25th International Conference on Noise and Vibration engineering (ISMA2012).

IGG™/AutoGrid5™ v11.1 (n.d) (Report).

Kailasanath K. (2003). Recent developments in the research on pulse detonation engines. AIAA Journal. 41: 145–159. https://doi.org/10.2514/2.1933

Kailasanath K. (2017). Recent Developments in the Research on Rotating-Detonation-Wave Engines. In: 55th AIAA Aerospace Sciences Meeting.

Kaiser S., Donnerhack S., Lundbladh A., and Seitz A. (2015). A Composite Cycle Engine Concept with Hecto-Pressure Ratio. In: 51st AIAA/SAE/ASEE Joint Propulsion Conference.

Klinger H., Lazik W., and Wunderlich T. (2008). The Engine 3E Core Engine. Volume 1: Aircraft Engine; Ceramics; Coal, Biomass and Alternative Fuels; Manufacturing, Materials and Metallurgy; Microturbines and Small Turbomachinery.

Klinger H., Bake S., Vogt H.-F., Knieschke D., and Schober P. (2011). Altitude Testing of the E3E Core Engine. Volume 1: Aircraft Engine; Ceramics; Coal, Biomass and Alternative Fuels; Wind Turbine Technology.

Lane F. (1956). System mode shapes in the flutter of compressor blade rows. Journal of the Aeronautical Sciences. 23: 54–66. https://doi.org/10.2514/8.3502

Li Z., Yang W., and Yuan H. (2016). Vibration analysis of aeroengine blisk structure based on a prestressed CMS super-element method. Shock and Vibration. 2016: 1–10. https://doi.org/10.1155/2016/1021402

Liu Z., Braun J., and Paniagua G. (2017). Performance of axial turbines exposed to large fluctuations. In: 53rd AIAA/SAE/ASEE Joint Propulsion Conference.

Lu F. K. and Braun E. M. (2014). Rotating detonation wave propulsion: Experimental challenges, modeling, and engine concepts. Journal of Propulsion and Power. 30: 1125–1142. https://doi.org/10.2514/1.B34802

Mao Z. and Kielb R. E. (2017). Interaction of Concurrent Forced Response and Flutter Phenomena in a Compressor Stage. Volume 7B: Structures and Dynamics.

Mayorca M. A., Vogt D. M., Mårtensson H., Andersson C., and Fransson T. H. (2012). Uncertainty of Forced Response Numerical Predictions of an Industrial Blisk: Comparison With Experiments. Volume 7: Structures and Dynamics, Parts A and B.

McClearn M. J., Polanka M. D., Lapp K., Mataczynski M. R., Schauer F. R., and Paxson D. E. (2016). The Testing of a Small-Scale Wave Rotor for Use as a Modified Brayton-Cycle Engine. In: 52nd AIAA/SAE/ASEE Joint Propulsion Conference.

Meitner P. L., Boruta M., and Jerovsek J. (2006). The Nutating Engine-Prototype Engine Progress Report and Test Results (Report).

Menter F. R. (1994). Two-equation eddy-viscosity turbulence models for engineering applications. AIAA Journal. 32: 1598–1605. https://doi.org/10.2514/3.12149

Pandey K. M. and Debnath P. (2016). Review on recent advances in pulse detonation engines. Journal of Combustion. 2016: 1–16. https://doi.org/10.1155/2016/4193034

Paxson D. E. and Naples A. (2017). Numerical and Analytical Assessment of a Coupled Rotating Detonation Engine and Turbine Experiment. In: 55th AIAA Aerospace Sciences Meeting.

Peitsch D., Poensgen C., and Mueck B. (2005). Unsteady Flow Investigations and Their Recent Challenges in Compressor Design. Volume 6: Turbo Expo 2005, Parts A and B.

Piperno S. and Farhat C. (2001). Partitioned procedures for the transient solution of coupled aeroelastic problems - Part II: energy transfer analysis and three-dimensional applications. Computer Methods in Applied Mechanics and Engineering. 190: 3147–3170. https://doi.org/10.1016/S0045-7825(00)00386-8

Platzer M. F., Carta F. O., North Atlantic Treaty Organization, Advisory Group for Aerospace Research and Development, Propulsion and Energetics Panel, et al. (1987). AGARD Manual on Aeroelasticity in Axial-flow Turbomachines: Structural dynamics and aeroelasticity. North Atlantic Treaty Organization, Advisory Group for Aerospace Research and Development.

Rasheed A., Furman A., and Dean A. (2005). Experimental Investigations of an Axial Turbine Driven by a Multi-Tube Pulsed Detonation Combustor System. In: 41st AIAA/ASME/SAE/ASEE Joint Propulsion Conference Exhibit.

Rasheed A., Furman A. H., and Dean A. J. (2009). Pressure measurements and attenuation in a hybrid multitube pulse detonation turbine system. Journal of Propulsion and Power. 25: 148–161. https://doi.org/10.2514/1.31893

Reichel T. G., Schäpel J.-S., Bobusch B. C., Klein R., King R., and Paschereit C. O. (2016). Shockless explosion combustion: Experimental investigation of a new approximate constant volume combustion process. Journal of Engineering for Gas Turbines and Power. 139: 021504. https://doi.org/10.1115/1.4034214

Rhie C. M. and Chow W. L. (1983). Numerical study of the turbulent flow past an airfoil with trailing edge separation. AIAA Journal. 21: 1525–1532. https://doi.org/10.2514/3.8284

Roache P. J. (1994). Perspective: A method for uniform reporting of grid refinement studies. Journal of Fluids Engineering. 116: 405. https://doi.org/10.1115/1.2910291

Roy G. D., Frolov S. M., Borisov A. A., and Netzer D. W. (2004). Pulse detonation propulsion: challenges, current status, and future perspective. Progress in Energy and Combustion Science. 30: 545–672. https://doi.org/10.1016/j.pecs.2004.05.001

Saiz G. (2008). Turbomachinery Aeroelasticity Using a Time-linearised Multi Blade-row Approach (Report). https://books.google.de/books?id=IcHjjgEACAAJ.

Schrape S., Nipkau J., Kühhorn A. and Beirow B. (2008). Application of Aeroelastic Methods in Compressor Cascade Configurations Using Commercial Code Coupling. Volume 4: Fluid-Structure Interaction.

Sever I. A. (2004). EXPERIMENTAL VALIDATION OF TURBOMACHINERY BLADE VIBRATION PREDICTIONS (Report).

Silkowski P. D. and Hall K. C. (1997). A Coupled Mode Analysis of Unsteady Multistage Flows in Turbomachinery. Volume 4: Manufacturing Materials and Metallurgy; Ceramics; Structures and Dynamics; Controls, Diagnostics and Instrumentation; Education; IGTI Scholar Award.

Taki H., Hirota N., Matsuoka K., Kawasaki A., Kasahara J., et al. (2017). Pulse Detonation Operation at Kilohertz Frequency. International Colloquium on the Dynamics of Explosions and Reactive Systems (ICDERS).

Thomas D. L. (1979). Dynamics of rotationally periodic structures. International Journal for Numerical Methods in Engineering. 14: 81–102. https://doi.org/10.1002/nme.1620140107

Van Zante D., Envia E., and Turner M. G. (2007). The Attenuation of a Detonation Wave by an Aircraft Engine Axial Turbine Stage. In: 18th AIAA International Symposium on Air-Breathing Engines. Beijing.

Vogt D. (2005). Experimental Investigation of Three-Dimensional Mechanisms in Low-Pressure Turbine Flutter (Report).

Wildheim S. J. (1979). Excitation of rotationally periodic structures. Journal of Applied Mechanics. 46: 878. https://doi.org/10.1115/1.3424671

Zhang X., Wang Y., and Xu K. (2012). Mechanisms and key parameters for compressor blade stall flutter. Journal of Turbomachinery. 135: 024501. https://doi.org/10.1115/1.4007441

Zhao F., Nipkau J., and Vahdati M. (2015). A Simple Low-Fidelity Model for Embedded Blade Row Flutter Prediction. Volume 7B: Structures and Dynamics.

Zhou R., Wu D., and Wang J. (2016). Progress of continuously rotating detonation engines. Chinese Journal of Aeronautics. 29: 15–29. https://doi.org/10.1016/j.cja.2015.12.006